CHEMISTRY OF MATERIALS

pubs.acs.org/cm

Article

Thermodynamics of Sodium−Lead Alloys for Negative Electrodes from First-Principles

Published as part of Chemistry of Materials virtual special issue "C. N. R. Rao at 90".

Damien K. J. Lee, Zeyu Deng, Gopalakrishnan Sai Gautam, and Pieremanuele Canepa*

Cite This: https://doi.org/10.1021/acs.chemmater.4c00592

Read Online

ACCESS | Metrics & More | Article Recommendations | Supporting Information

ABSTRACT: Metals, such as tin, antimony, and lead (Pb) have garnered renewed attention for their potential use as alloyant-negative electrode materials in sodium (Na)-ion batteries (NIBs). Despite Pb's toxicity and its high molecular weight, lead is one of the most commonly recycled metals, positioning Pb as a promising candidate for a cost-effective, high-capacity anode material. Understanding the miscibility of Na into Pb is crucial for the development of high-energy density negative electrode materials for NIBs. Using a first-principles multiscale approach, we analyze the thermodynamic properties and estimate the Na-alloying voltage of the Na−Pb system by constructing the compositional phase diagram. In the Na−Pb system, we elucidate the phase boundaries of important phases, such as Pb-rich face-centered cubic and β-$NaPb_3$, thereby improving our understanding of the phase diagram of the Na−Pb alloy. Due to the strong ordering tendencies of the Na−Pb intermetallics (such as NaPb, Na_5Pb_2, and $Na_{15}Pb_4$), we do not observe any solid-solution behavior at intermediate and high Na concentrations.

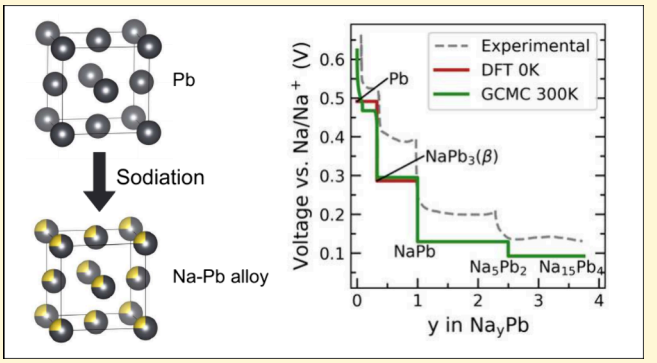

INTRODUCTION

Sodium (Na)-ion batteries (NIBs) present a cost-effective alternative to their lithium (Li)-ion counterparts, primarily owing to the greater natural abundance of Na and its compatibility with aluminum current collectors, as opposed to the more expensive and heavier copper ones.[1] The reduced dependence on expensive materials, such as Li or cobalt, positions the NIB technology as particularly well-suited for large-scale energy storage applications, offering an economically viable solution to address the challenges posed by intermittent renewable energy sources.[2−4]

Unlike in Li-ion electrochemistry, graphite cannot be used as a negative electrode in NIBs since Na does not reversibly intercalate into graphite at low voltages.[5] Hence, hard carbon-based materials are generally used as the negative electrode for NIBs,[6,7] achieving capacities of 300−350 mAh/g.

Sodium-based alloys, specifically with elements of groups 14 and 15, can potentially offer higher capacities than hard carbon materials, in which Na undergoes an alloying reaction with another element to form stable phases. With high theoretical capacities of 847, 660, and 2596 mAh/g, respectively, tin, antimony, and phosphorus have been investigated as negative electrode materials in Na batteries.[8−11] However, one major drawback of alloy-type electrodes is the large volume change during cycling, causing electrode pulverization, loss of contact with the current collector, and rapid capacity fading.[12] Further, the active electrode material can fracture and disintegrate, which have been experimentally observed in many *in situ* studies of lithium-ion battery (LIB) and NIB negative electrodes, such as silicon and tin.[13−15]

Despite its inherent toxicity and high molecular weight, lead (Pb) has been used in batteries ever since the invention of the lead-acid battery in 1859. Notably, lead-acid batteries are currently recycled at a rate of 99%,[16,17] charting them as one of the world's most recycled technological devices. Thus, despite the limitations, lead can be explored as a cost-effective alloy-type negative electrode material for large-scale NIB-based energy storage solutions.

So far, there have been limited investigations of using lead as a negative electrode in NIBs. Jow et al. were the first to investigate the electrochemical reaction of Na with Pb,[18] where the authors reported a series of intermetallics that form during the alloying of Na with Pb, following the sequence Pb → $NaPb_3$ → NaPb → Na_5Pb_2 → $Na_{15}Pb_4$.[18] These phases agree

Received: March 1, 2024
Revised: June 21, 2024
Accepted: June 24, 2024

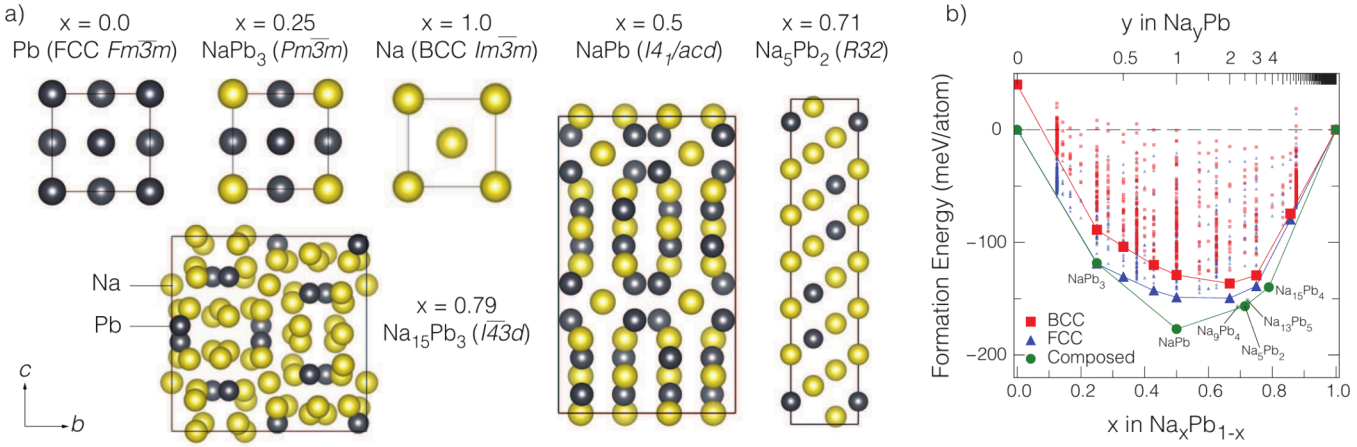

Figure 1. a) Known crystal structures of Na−Pb intermetallics. Na atoms are colored in yellow and Pb atoms in black. x represents Na content in Na_xPb_{1-x}. **b)** Convex hull of the intermetallic phases (green circles), FCC orderings (blue triangles), and BCC orderings (red squares). The references used are the FCC structure for pure Pb and the BCC structure for pure Na.

well with the experimental phase diagram of the Na−Pb system.[19] In its fully sodiated phase, $Na_{15}Pb_4$ provides a theoretical capacity of 485 mAh/g.

More recently, Darwiche et al.[20] reported noteworthy capacity retention (464 mAh/g) and Coulombic efficiency (99.99%) over 50 cycles for a 98 wt % Pb as an electrode for NIBs. Through *in situ* X-ray diffraction (XRD), the authors observed successive phase transitions during the sodiation of Pb,[20] highlighting the absence of a solid solution behavior. Importantly, the authors reported the formation of an intermediate phase with lower Na content, namely Na_9Pb_4 (Na: Pb = 2.25), instead of Na_5Pb_2 (2.50).[20]

To date, the extent of spontaneous Na−Pb mixing has not been fully elucidated in the Na−Pb system, particularly in the Pb-rich chemical space.[19] In particular, the phase boundaries of the so-called β-phase, $NaPb_3$, are not resolved over a wide temperature range in the current Na−Pb phase diagram. Thus, we investigate the thermodynamics of the Na−Pb system at varying temperatures, through a multiscale computational approach.

We explore the solubility of Na within the Pb face-centered cubic (FCC) structure as a function of temperature, and derive the temperature-dependent voltage profile of the Na-alloying reaction with Pb, through a combination of density functional theory (DFT),[21,22] cluster expansion (CE),[23] and semigrand canonical Monte Carlo (GCMC) simulations. Importantly, we show evidence of solid solution behavior in the low sodium compositions and also unveil the phase boundaries of phases that occur in the Pb-rich region, which are not well-defined in existing phase diagrams. Our study provides a comprehensive understanding of the thermodynamics of Na alloying with Pb, which unlocks potential strategies for enhancing the reversible capacities and compatibility with electrolytes of alloy-type negative electrode materials in NIBs.

RESULTS

The intermetallic structures of all experimentally known Na−Pb phases are illustrated in Figure 1a. Using DFT, the formation energies of all intermetallic Na−Pb orderings are calculated to evaluate their phase stability, which enables the construction of the binary phase diagram at 0 K —the "convex hull" of the Na−Pb system, in Figure 1b. The lattice parameters of the optimized structures and the details of our DFT calculations are found in the Methods Section and Section S1 of the Supporting Information (SI).

Since Na crystallizes as a body-centered cubic (BCC) structure and Pb in an FCC system, Na−Pb orderings of Pb in BCC Na (red squares in Figure 1b), and Na in FCC Pb (blue triangles), respectively, were considered. In mapping the Na−Pb binary systems with DFT, known Na−Pb orderings (Figure 1a) at intermediate compositions whose structures deviate from either that of BCC Na or FCC Pb were also considered.

The overall convex hull (green circles in Figure 1), minimizing the formation energy of the Na−Pb orderings was constructed with the phases stable at room temperature as reference configurations, namely, FCC for lead and BCC for Na. Thus, the reference configurations for the FCC (BCC) convex hull are pure Pb and pure Na in FCC (BCC) structures. Na−Pb structures forming the convex hull in Figure 1b are the reflection of stabilizing enthalpic conditions driven by the formation of stable bonds between Na and Pb atoms.

In Figure 1b, the Na_9Pb_4 ($P6_3/mmc$) and $Na_{13}Pb_5$ ($P6_3/mmc$) phases[24,25] appear metastable on the overall convex hull (green line), with relatively small decomposition energies of ~1.51 and ~3.41 meV/atom, respectively. The low decomposition energies indicate that these phases may be entropy stabilized, and hence observed at room temperature.

As illustrated in Figure 1b, the BCC convex hull is consistently above both the FCC and the overall convex hulls. The high formation energies of the Na−Pb orderings in the BCC structure indicate the poor thermodynamic stability of this phase, especially for intermediate Na−Pb compositions. This suggests that the BCC-based phases are unlikely to be observed in experiments, apart from high Na-content regions (e.g., $x > 0.9$ in Na_xPb_{1-x}) of the phase diagram.

The FCC and the overall convex hull share a common tangent line between x = 0 and x = 0.25, which is to be expected since the $NaPb_3$ phase ($Pm\bar{3}m$) is an FCC-based ordering, where the corner (face-centered) sites of the cube are occupied by Na (Pb, see Figure 1a). Other Na−Pb orderings in the FCC hull remain above the overall convex hull, indicating the strong thermodynamic stability of the ordered intermetallic phases. In addition, the FCC polymorph of Na metal is only slightly metastable, by ~0.51 meV/atom, versus its BCC ground-state.

https://doi.org/10.1021/acs.chemmater.4c00592
Chem. Mater. XXXX, XXX, XXX−XXX

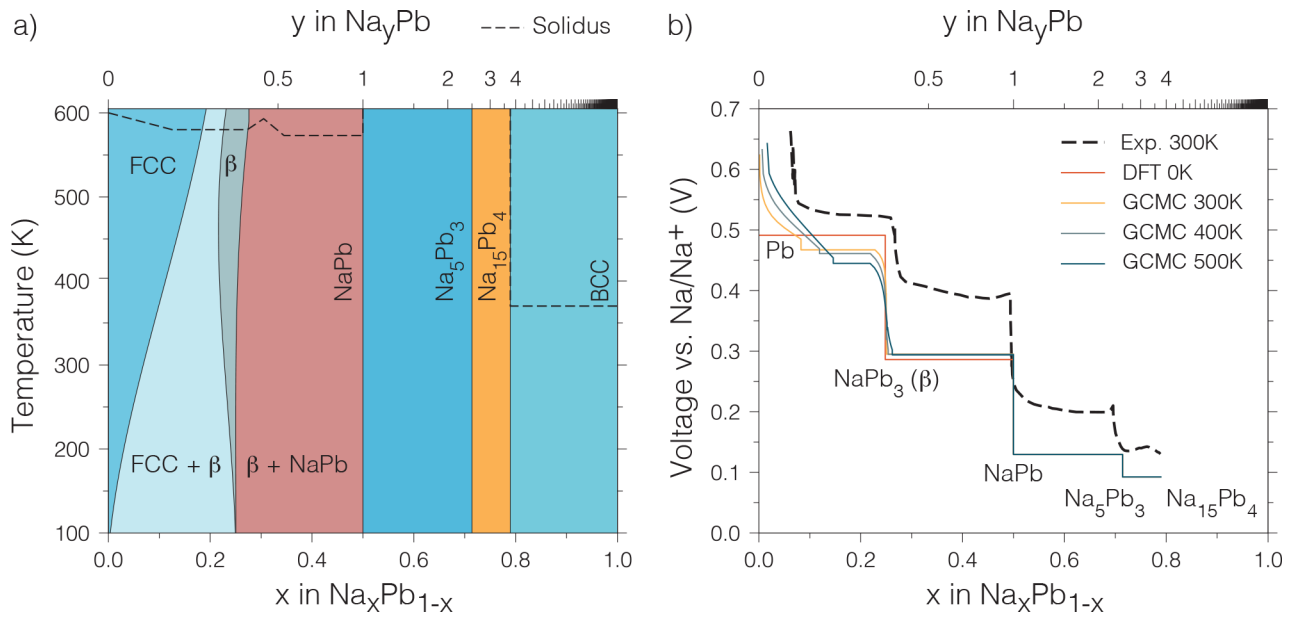

Figure 2. a) Predicted temperature−composition phase diagram of the Na−Pb system. The dashed lines indicate the solidus lines, as taken from the experimental phase diagram of ref 19. **b)** Computed voltage (Volts vs. Na/Na^+) curves as a function of x in Na_xPb_{1-x} at different temperatures (T = 0K, 300, 400, and 500 K). The experimental voltage of the Na-dealloying from ref 18. (© The Electrochemical Society. Reproduced with permission of IOP Publishing Ltd. All rights reserved) is superimposed on the computed voltage curves as the dashed black line. Since the amount of Pb remains constant during cycling, the number of Na alloyed per Pb atom (i.e., y in Na_yPb) is included at the top of both panels for convenience.

The CE approach, introduced by Sanchez et al.[23] was used to parametrize the DFT formation energies based on the FCC crystal structure and the associated convex hull. Relying on 975 symmetrically nonequivalent Na−Pb orderings, we constructed a CE to enable the fast evaluation of the formation energy of any arbitrary Na/Pb configuration within the FCC structure.[26−28] Details of the CE model are in Section S3 of the SI.

The converged CE features 33 unique effective cluster interactions (ECIs) of which are 1 constant term, 1 point term, 6 pairs, 12 triplets, and 13 quadruplets. The transferability of the CE was assessed by the leave-one-out cross-validation (LOOCV) score of the CE model, which was ∼4.60 meV/atom. The root-mean-square error (RMSE) of the CE model, ∼ 3.52 meV/atom indicates the quality of the CE fit, with the CE reproducing all ground states predicted by DFT (see Figure S1 in the Supporting Information). Subsequently, we combined the CE with semi-GCMC simulations to predict the free energies of an extended range of Na compositions at varying temperatures.

The construction of the phase diagram of Figure 2a, and hence the location of the phase boundaries requires the identification of discontinuities in the variation of Na concentration (x) versus the sodium chemical potential (μ_{Na}). Importantly, we removed the numerical hysteresis arising from GCMC simulations through thermodynamic integration (see section S4 in SI).[27,29] Known ordered Na−Pb intermetallics, such as NaPb, Na_5Pb_2, and $Na_{15}Pb_4$ of Figure 1b, were integrated with the GCMC calculations to determine their respective free energies with respect to the FCC phases (see Section S4 of the Supporting Information). This procedure allowed us to obtain a complete phase diagram of Figure 2a.

Remarkably, Figure 2a reproduces with great accuracy the main features of the experimental phase diagram.[19] The computed phase diagram of Figure 2a contains two single-phase regions described as *i*) FCC, Na atoms in the Pb matrix forming a solid solution, *ii*) β ($NaPb_3$), a cubic phase consisting of FCC sites with a narrow range of solubility (Figure 2a). The β and the FCC Pb solid solution are separated by a miscibility gap. GCMC simulations demonstrated that the miscibility gap closes at temperatures higher than ∼650 K, which is well beyond the solidus line (dashed black lines) and hence not shown in Figure 2a.

Other known intermetallics,[30] such as NaPb ($I4_1/acd$), Na_5Pb_2 ($R\bar{3}m$), $Na_{15}Pb_4$ ($I\bar{4}3d$) appear as "line compounds" on the phase diagram of Figure 2a, since we did not include the effect of off-stoichiometry for these compounds in our calculations. Nevertheless, such compositions also appear as line compounds in the experimental Na−Pb phase diagram.[19]

The strong tendency of Na−Pb ordering in the $Na_{15}Pb_4$ phase and the significant size difference between Na and Pb atoms suppress the solubility of Pb within BCC Na-metal (x = 1). Therefore, the Na-rich BCC phase appears as a line compound in the phase diagram in the limit $x \rightarrow 1$, with no solubility of Pb in Na observed up to 600 K.

Having established the Na−Pb phase diagram, we use this knowledge to derive voltage curves at variable temperatures for Na alloying with Pb, which are useful for guiding the interpretation of electrochemical experiments with the Na−Pb alloy system. Figure 2b illustrates the computed alloying voltage profile across the whole Na compositional region at selected temperatures of 0 K, 300 K 400 K, and 500 K. Since the Pb present on the electrode can be assumed to be immobile, and hence the amount of Pb to be constant during battery cycling, we also plot the voltage profile as a function of the number of atoms per Pb atom (i.e., y in Na_yPb).

Note that we obtained the voltage profile at 0 K directly from DFT calculations of Figure 1b), while voltage profiles at temperatures >0 K were determined by calculating Gibbs energies through thermodynamic integration (Section S4 in

https://doi.org/10.1021/acs.chemmater.4c00592
Chem. Mater. XXXX, XXX, XXX−XXX

SI). At 0 K, there are four plateaus, corresponding to the respective two-phase regions: *i*) Pb+$NaPb_3$ (~0.49 V vs Na/Na+), *ii*) $NaPb_3$+NaPb (~0.29 V), *iii*) NaPb+Na_5Pb_2 (~0.13 V), and *iv*) Na_5Pb_2+$Na_{15}Pb_4$. Expectedly, the plateau Na_5Pb_2+$Na_{15}Pb_4$ is located at a very low voltage (~0.09 V vs Na/Na^+).

As the effect of temperature is introduced, subtle variations emerge in the voltage profile compared to the 0 K profile, in particular, in regimes of low Na concentrations ($y < 0.5$). For example, at 300 K and $0 < y < 0.5$, a distinct single-phase region emerges where Na dissolves into the FCC matrix of Pb. The voltage curve for the alloying reaction exhibits a smooth monotonic variation up to the solubility limit of Na. Likewise, the same solid solution behavior is observed corresponding to the single-phase β region, occurring within a narrow Na composition range ($0.23 < y < 0.33$).

With increasing temperature, the width of the two-phase region enclosed between the FCC and the β phases in Figure 2a) diminishes, as indicated by the reduction of the voltage plateau in Figure 2b). However, as elevated temperatures do not expand the width of the line compounds (e.g., NaPb, Na_5Pb_3, and $Na_{15}Pb_4$, other voltage plateaus in the region $0.35 < y < 3.75$ remain practically unaffected by temperature. This is to be expected since the configurational entropy of the ordered intermetallics is 0, resulting in no appreciable temperature effects on the Gibbs energies of formation of these phases.

The experimental voltage profile of the Na-dealloying reaction, reported by Jow et al.[18] is superimposed on the calculated voltage profiles. In general, there is a good (qualitative) agreement between the experimental and theoretical sodiation voltages, with the computed voltage profiles underestimating the experimental data by a systematic offset of ~0.1 V. The magnitude of this offset aligns with the previous report on anode materials for Na batteries.[31]

DISCUSSION

In this work, we investigated the thermodynamics governing the alloying of Na into Pb by implementing a multiscale approach based on first-principles calculations, the cluster expansion formalism, and Monte Carlo simulations. The alloying reaction of Pb with Na holds potential for use in the negative electrode in Na batteries. Unlike intercalation-type electrodes, alloy-type (or conversion-type) electrodes undergo the formation of entirely new phases during reversible sodiation. Understanding the phase changes occurring within the electrode is essential for identifying the limitations imposed by the reaction mechanism, such as practical losses related to initial particle morphology, synthetic approaches, and electrode preparations.[32] Here, through the acquired knowledge of the compositional Na−Pb phase diagram, we have identified the thermodynamically stable phases and elucidated the reaction mechanisms occurring during the alloying process manifested in the battery cycling process. Notably, our work sheds light on the phase boundaries of the β phase, an important detail that was not identified in previous explorations of the Na−Pb phase diagram.

The computed phase diagram compares favorably with the existing experimentally determined phase diagram. For instance, the Na solubility in the FCC matrices of pure Pb and the β phase is observed, while the remaining intermetallic phases NaPb, Na_5Pb_2 and $Na_{15}Pb_4$ appear as line compounds. At low Na concentrations, a solid solution is formed in which Na occupies the FCC sites of the Pb matrix. With increasing temperature, higher configurational entropy results in a lower Gibbs Free energy, stabilizing the mixing process and increasing the solubility limit of Na. The formation of the β-phase occurs when Na atoms simultaneously occupy the corner sites of the FCC lattice, resulting in an ordered phase with limited solubility. The miscibility gap between the FCC phase and β phase does not close at temperatures below its solidus temperature, which indicates the formation of biphasic regions of differing Na content within the electrode material during sodiation. We speculate that upon sodiation of Pb-FCC, the formation of the β phase is likely dominated by vacancy diffusion. Therefore, if the sodiation of the Pb electrode occurs at high rates, thus faster than the time allowed for Na atoms to order, the β phase may be suppressed and may not be observed during cycling. Therefore, fast cycling rates may bypass the β-phase $NaPb_3$, and form a two-phase region between FCC and NaPb phases. Suppressing the β-phase will also increase the solubility limit of Na in the FCC phase.

At Na concentrations $x > 0.5$, it is likely that the metastable Na_9Pb_4 phase forms instead of the Na_5Pb_2, as the voltage step appears closer to $y = 2.25$ than $y = 2.5$ in Jow et al.'s experimental findings.[18] This finding is corroborated by the in situ study reported by Darwiche et al.[20] There are several reasons why the Na_9Pb_4 phase is not observed in our results. First, at 0 K, Na_9Pb_4 does not appear as a ground state but with proximity to the convex hull (~1.51 meV/atom). With increasing temperature, vibrational entropy might play a role in stabilizing the Na_9Pb_4 phase. Second, our model does not include vibrational contributions in determining the Gibbs energies. Third, the formation of Na_9Pb_4 might be more kinetically favorable over Na_5Pb_2, which results in its observation during cycling.

At higher Na concentrations, phase separation prevails, with no solid solution behavior due to the formation of ordered intermetallic compounds. Here, the enthalpy of the formation of these compounds dominates, and configurational entropy does not affect the stability of these phases. Full sodiation of pure Pb results in the formation of a stable $Na_{15}Pb_4$ compound, corresponding to a theoretical capacity of ~485 mAh/g, with 3.75 Na per Pb atom.

Arguably, the primary drawback limiting the use of alloy-type anodes is the pronounced volume change occurring during charge/discharge processes. Upon repeated Na cycling, the substantial volume fluctuation can lead to the pulverization of electrode materials and subsequent capacity fading.[33] In Figure 3, we quantified the volume expansion of the Pb electrode as a function of the number of Na atoms inserted. The volume increase within the electrode appears nearly proportional to the quantity of Na alloyed with Pb, as evident from Figure 3. A linear fit of Figure 3 demonstrates that the volume expands with a rate of ~95.5% per sodium atom alloyed with respect to FCC Pb. The fully sodiated phase of $Na_{15}Pb_4$ corresponds to an exceedingly high volume increase of ~366.6%.

Notwithstanding the large volume variation incurred by Na−Pb alloying reactions, the volume expansion estimated in Figure 3 appears lower than that of other commonly used alloy materials, such as Sn and Sb, which exhibit expansions of 423% and 390%, respectively, with respect to the fully sodiated phases ($Na_{15}Sn_4$ and Na_3Sb).[34] This relatively lower volume change in Pb compared to other alloys suggests its potential utility as a high volumetric energy density material with longer cycle life. Further optimization in particle size, morphology,

https://doi.org/10.1021/acs.chemmater.4c00592
Chem. Mater. XXXX, XXX, XXX−XXX

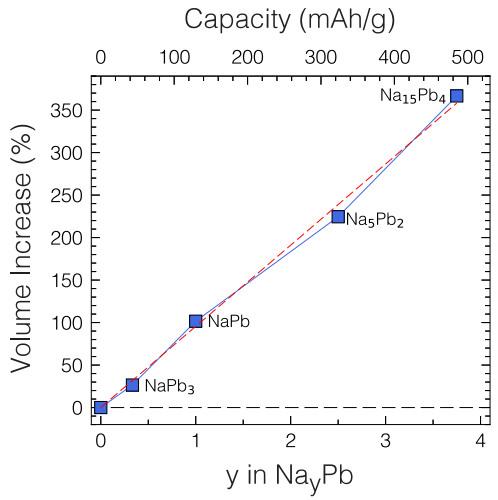

Figure 3. Volume expansion of the alloying reaction (in % increase) as a function of the amount of Na alloyed per Pb atom. The theoretical capacity of the Pb electrode is indicated. The percent increase is calculated with respect to pure FCC Pb, as indicated by the black dashed line. A linear fit is indicated by the red dashed line, with the equation: Percent Increase = 95.5 × (y in Na_yPb).

and blending with other materials, could potentially alleviate the adverse effects of volume changes,[9] a strategy that has been successfully employed in silicon nanowires for LIBs,[35,36] as well as nanostructures in Sn and Bi−Sb alloys for NIBs.[37,38]

CONCLUSION

The phase behavior of the full compositional space of the Na−Pb binary system was investigated using a multiscale approach. The computed diagram accurately captured the thermodynamically stable intermetallic phases reported in experimental studies. The phase boundaries of the $NaPb_3$ phase, are identified, addressing a gap in the known Na−Pb phase diagram. At low Na concentrations, the computed phase diagram highlights the significant solubility of Na within the FCC Pb matrix, especially at higher temperatures, resulting in sloped voltage profiles as Na alloys with FCC Pb. Due to the strong ordering tendencies of the Na−Pb intermetallics (such as NaPb, Na_5Pb_2, and $Na_{15}Pb_4$), we do not observe any solid-solution behavior at intermediate and high Na concentrations.

Structural analysis revealed that the Na−Pb alloy expands up to 366.6% during full sodiation of Pb to $Na_{15}Pb_4$. This expansion is much reduced in magnitude compared to other negative electrode materials, e.g. Sn and Sb. Despite its high molecular weight, Pb can deliver a high theoretical capacity of 485 mAh/g, surpassing current commercial hard carbon materials commonly used in Na-ion batteries. Coupled with its high recycling rate, Pb anodes emerge as a promising candidate for a low-cost negative electrode material in bulk or blended with hard carbons. Our work is an important contributor to the design and engineering of alloy-type negative electrodes for NIBs.

METHODS

First-principles Calculations. The Vienna Ab initio Simulation Package (VASP)[39,40] was used for the DFT collinear spin-polarized calculations for all structures. The generalized gradient approximation-type Perdew−Burke−Ernzerhof (PBE) functional was used to approximate the unknown exchange-correlation contribution in DFT.[41] The PBE functional was selected as it gives a reasonable trade-off between accuracy and computational costs and its efficacy for accurate calculations of various Na-based battery materials within our research group.[29,42] Notably, PBE enabled us to carry out 1,200 distinct DFT geometry optimizations.

The projector augmented wave (PAW) potentials described the core electrons.[43,44] The PAW potentials used were Na `08Apr2002` $3s^13p^0$ and Pb `08Apr2002` $6s^26p^2$. Valence electrons were represented using plane waves up to an energy cutoff of 520 eV. A Γ-centered Monkhorst−Pack k-point mesh with a grid density of 5000/(number of atoms) was used, which was determined after appropriate convergence tests. Although these materials are non-magnetic, all calculations were initialized as ferromagnetic.[45] The DFT total energy of each structure was converged to within 10^{-5} eV/cell, and atomic forces within 10^{-2} eV· $Å^{-1}$. Spin−orbit coupling (SOC) effects were not considered in our calculations as we do not observe any significant differences with the inclusion of SOC effects (see Section S2 of Supporting Information).

Energies of Mixing and Cluster Expansion. The enthalpy of Na mixing into Pb was approximated by the formation energy. The formation energy per atom (E_f) of the alloy at any sodium composition (x) can be calculated with eq 1.

$$E_f = E(Na_xPb_{1-x}) - [xE(Na) + (1 - x)E(Pb)] \quad (1)$$

where $E(Na_xPb_{1-x})$ is the DFT total energy of the alloy at a sodium atomic composition x, E (Na) and E (Pb) are the DFT total energies (per atom) of Na and Pb metals in their BCC and FCC phases, respectively.

In the cluster expansion (CE) formalism, the formation energy E_f of a particular Na−Pb structure is a function of the Na and Pb occupation in a generic FCC lattice, and eq 2.

$$E_f(\vec{\sigma}) = V_0 + \sum_i V_i\sigma_i + \sum_{i,j} V_{i,j}\sigma_i\sigma_j + \sum_{i,j,k} V_{i,j,k}\sigma_i\sigma_j\sigma_k \quad (2)$$

where (V_i, $V_{i,j}$, and $V_{i,j,k}$) are the effective cluster interactions (ECIs) of the point term, pair, and triplet clusters, respectively. σ is the occupation variable of each site in the crystal, which is +1 if the site is occupied by Na and −1 if the site is occupied by Pb. Each ECI includes the multiplicity of the cluster and is fit to a set of DFT training data. The CE model was used to construct all symmetrically distinct pairs, triplets, and quadruplets in the FCC cell within a radius of 12, 8, and 7.5 Å, respectively.

The CE model was fit using the Clusters Approach to Statistical Mechanics (CASM) code.[26−28] To fit the CE model, the Na/Pb configurations of different compositions were enumerated up to a maximum supercell size of 8 times the primitive cell. Only structures with a basis deformation of <0.1 were included in the CE fit. Note, 0.1 is a typical threshold used to identify structures that match the primitive unit cell. The basis deformation is determined by the mean-square atomic displacement relative to the positions of the atoms in the primitive FCC lattice. During the CE fit, each structure's weights were optimized using Bayesian Optimization with Gaussian Processes, which minimized the error between the DFT hull and the predicted CE hull (Figure S2 of Supporting Information).

Monte Carlo Simulations. In a grand-canonical ensemble, the composition and energy of the system with a fixed number of sites were sampled while the temperature (T) and the Na chemical potential μ_{Na} were varied. The chemical potentials were referenced to the pure FCC Pb and Na phases, for which $\mu_{Na} = \mu_{Pb} = 0$. Semigrand canonical Monte Carlo (GCMC) simulations were performed using the CASM package. A 16 × 16 × 16 (4,096 atoms) supercell was used for these simulations. GCMC scans were performed in the chemical potential (μ) and temperature (T) space. The scan started at T = 5K and up to 705 K with a step ΔT = 5K at μ = −0.6, −0.3, −0.1, 0.1, 0.4, and 0.6 eV/atom. These values of μ correspond to the initial six ground-state structures on the FCC convex hull (x = 0, 0.25, 0.5, 0.67, 0.75, 1). At every T, μ was scanned forward and backward in a chemical potential range (μ = −0.6 to 0.6 eV/atom) with a step size of $\Delta\mu$ = 0.01 eV/atom In general, μ was scanned across 5

https://doi.org/10.1021/acs.chemmater.4c00592
Chem. Mater. XXXX, XXX, XXX−XXX

concentration ranges ($-0.6 < \mu < -0.3$, $-0.3 < \mu < -0.1$, $-0.1 < \mu < 0.1$, $0.1 < \mu < 0.4$, $0.6 < \mu < 0.6$).

Voltage Profiles. The (de)alloying reaction of Na into(from) Pb metal can occur through the reversible reaction eq 3:

$$\mathrm{Na}_x\mathrm{Pb} + (y - x)\mathrm{Na} \xleftrightarrow{-\Delta G} \mathrm{Na}_y\mathrm{Pb} \tag{3}$$

where x and y represent the initial and final Na content per Pb atom, and $-\Delta G$ is the change in Gibbs free energy of the reaction.

The voltage of alloying a particular composition of Na in Pb metal is calculated using eq 4:

$$V = -\frac{\Delta G}{nF} = -\frac{G_{f,\mathrm{Na}_y\mathrm{Pb}} - G_{f,\mathrm{Na}_x\mathrm{Pb}}}{y - x} \tag{4}$$

where G_f is the Gibbs free energy (in eV) to form a Na−Pb alloy at a particular composition and is calculated after thermodynamic integration of the grand-canonical potential Φ at temperature T:

$$G \approx E - \mathrm{TS} = \Phi + \mu x \tag{5}$$

■ ASSOCIATED CONTENT

Supporting Information

The Supporting Information is available free of charge at https://pubs.acs.org/doi/10.1021/acs.chemmater.4c00592.

Details of the calculated lattice parameters of all intermetallics, calculation of formation energies with first-principles methods, details on the cluster expansion and Monte Carlo simulations, free energy integration, and voltage calculations (PDF)

■ AUTHOR INFORMATION

Corresponding Author

Pieremanuele Canepa − *Department of Electrical and Computer Engineering, Houston, Texas 77204, United States; Texas Center for Superconductivity, University of Houston, Houston, Texas 77204, United States; Department of Materials Science and Engineering, National University of Singapore, 117575, Singapore;* orcid.org/0000-0002-5168-9253; Email: pcanepa@uh.edu

Authors

Damien K. J. Lee − *Department of Materials Science and Engineering, National University of Singapore, 117575, Singapore;* orcid.org/0009-0006-1100-6477

Zeyu Deng − *Department of Materials Science and Engineering, National University of Singapore, 117575, Singapore;* orcid.org/0000-0003-0109-9367

Gopalakrishnan Sai Gautam − *Department of Materials Engineering, Indian Institute of Science, Bangalore 560012, India;* orcid.org/0000-0002-1303-0976

Complete contact information is available at: https://pubs.acs.org/10.1021/acs.chemmater.4c00592

Notes

The authors declare no competing financial interest.

■ ACKNOWLEDGMENTS

P.C. acknowledges funding from the National Research Foundation under its NRF Fellowship NRFF12-2020-0012. The Welch Foundation is acknowledged for providing P.C. a Robert A. Welch professorship at the Texas Center for Superconductivity. The computational work was performed on resources of the National Supercomputing Centre, Singapore (https://www.nscc.sg).

■ REFERENCES

(1) Kim, S.-W.; Seo, D.-H.; Ma, X.; Ceder, G.; Kang, K. Electrode Materials for Rechargeable Sodium-Ion Batteries: Potential Alternatives to Current Lithium-Ion Batteries. *Adv. Energy Mater.* **2012**, *2*, 710−721.

(2) Vaalma, C.; Buchholz, D.; Weil, M.; Passerini, S. A cost and resource analysis of sodium-ion batteries. *Nat. Rev. Mater.* **2018**, *3*, 1−11.

(3) Slater, M. D.; Kim, D.; Lee, E.; Johnson, C. S. Sodium-Ion Batteries. *Adv. Funct. Mater.* **2013**, *23*, 947−958.

(4) Palomares, V.; Serras, P.; Villaluenga, I.; Hueso, K. B.; Carretero-González, J.; Rojo, T. Na-ion batteries, recent advances and present challenges to become low cost energy storage systems. *Energy Environ. Sci.* **2012**, *5*, 5884−5901.

(5) Ge, P.; Fouletier, M. Electrochemical intercalation of sodium in graphite. *Solid State Ionics* **1988**, *28−30*, 1172−1175.

(6) Stratford, J. M.; Kleppe, A. K.; Keeble, D. S.; Chater, P. A.; Meysami, S. S.; Wright, C. J.; Barker, J.; Titirici, M.-M.; Allan, P. K.; Grey, C. P. Correlating Local Structure and Sodium Storage in Hard Carbon Anodes: Insights from Pair Distribution Function Analysis and Solid-State NMR. *J. Am. Chem. Soc.* **2021**, *143*, 14274−14286.

(7) Stevens, D. A.; Dahn, J. R. The Mechanisms of Lithium and Sodium Insertion in Carbon Materials. *J. Electrochem. Soc.* **2001**, *148*, A803.

(8) Hasa, I.; Mariyappan, S.; Saurel, D.; Adelhelm, P.; Koposov, A. Y.; Masquelier, C.; Croguennec, L.; Casas-Cabanas, M. Challenges of today for Na-based batteries of the future: From materials to cell metrics. *J. Power Sources* **2021**, *482*, 228872.

(9) Rudola, A.; Rennie, A. J. R.; Heap, R.; Meysami, S. S.; Lowbridge, A.; Mazzali, F.; Sayers, R.; Wright, C. J.; Barker, J. Commercialisation of high energy density sodium-ion batteries: Faradion's journey and outlook. *J. Mater. Chem. A* **2021**, *9*, 8279−8302.

(10) Stratford, J. M.; Mayo, M.; Allan, P. K.; Pecher, O.; Borkiewicz, O. J.; Wiaderek, K. M.; Chapman, K. W.; Pickard, C. J.; Morris, A. J.; Grey, C. P. Investigating Sodium Storage Mechanisms in Tin Anodes: A Combined Pair Distribution Function Analysis, Density Functional Theory, and Solid-State NMR Approach. *J. Am. Chem. Soc.* **2017**, *139*, 7273−7286.

(11) Marbella, L. E.; Evans, M. L.; Groh, M. F.; Nelson, J.; Griffith, K. J.; Morris, A. J.; Grey, C. P. Sodiation and Desodiation via Helical Phosphorus Intermediates in High-Capacity Anodes for Sodium-Ion Batteries. *J. Am. Chem. Soc.* **2018**, *140*, 7994−8004.

(12) Tian, Y.; Zeng, G.; Rutt, A.; Shi, T.; Kim, H.; Wang, J.; Koettgen, J.; Sun, Y.; Ouyang, B.; Chen, T.; Lun, Z.; Rong, Z.; Persson, K.; Ceder, G. Promises and Challenges of Next-Generation "Beyond Li-ion" Batteries for Electric Vehicles and Grid Decarbonization. *Chem. Rev.* **2021**, *121*, 1623−1669.

(13) Beaulieu, L. Y.; Eberman, K. W.; Turner, R. L.; Krause, L. J.; Dahn, J. R. Colossal Reversible Volume Changes in Lithium Alloys. *Electrochem. Solid-State Lett.* **2001**, *4*, A137.

(14) Liu, X. H.; et al. Anisotropic Swelling and Fracture of Silicon Nanowires during Lithiation. *Nano Lett.* **2011**, *11*, 3312−3318.

(15) Ying, H.; Han, W.-Q. Metallic Sn-Based Anode Materials: Application in High-Performance Lithium-Ion and Sodium-Ion Batteries. *Adv. Sci.* **2017**, *4*, 1700298.

(16) May, G. J.; Davidson, A.; Monahov, B. Lead batteries for utility energy storage: A review. *Journal of Energy Storage* **2018**, *15*, 145−157.

(17) Yanamandra, K.; Pinisetty, D.; Daoud, A.; Gupta, N. Recycling of Li-Ion and Lead Acid Batteries: A Review. *J. Indian Inst. Sci.* **2022**, *102*, 281−295.

(18) Jow, T. R.; Shacklette, L. W.; Maxfield, M.; Vernick, D. The Role of Conductive Polymers in Alkali-Metal Secondary Electrodes. *J. Electrochem. Soc.* **1987**, *134*, 1730.

(19) Lamprecht, G. J.; Dicks, L.; Crowther, P. Solubility of metals in liquid sodium. II. The system sodium-lead. *J. Phys. Chem.* **1968**, *72*, 1439−1441.
(20) Darwiche, A.; Dugas, R.; Fraisse, B.; Monconduit, L. Reinstating lead for high-loaded efficient negative electrode for rechargeable sodium-ion battery. *J. Power Sources* **2016**, *304*, 1−8.
(21) Hohenberg, P.; Kohn, W. Inhomogeneous Electron Gas. *Phys. Rev.* **1964**, *136*, B864−B871.
(22) Kohn, W.; Sham, L. J. Self-Consistent Equations Including Exchange and Correlation Effects. *Phys. Rev.* **1965**, *140*, A1133−A1138.
(23) Sanchez, J. M.; Ducastelle, F.; Gratias, D. Generalized cluster description of multicomponent systems. *Physica A* **1984**, *128*, 334−350.
(24) Ward, L.; Michel, K.; Wolverton, C. Three new crystal structures in the Na−Pb system: solving structures without additional experimental input. *Acta Crystallogr. A Found. Adv.* **2015**, *71*, 542−548.
(25) Weston, N.; Shoemaker, D.; Kuhi, L.; Tse, R. The crystal structures of three phases in the Pb-Na system. *Acat Crystallographica* **1957**, *10*, 775−775.
(26) Puchala, B.; Van der Ven, A. Thermodynamics of the Zr-O system from first-principles calculations. *Phys. Rev. B* **2013**, *88*, 094108.
(27) Puchala, B.; Thomas, J. C.; Natarajan, A. R.; Goiri, J. G.; Behara, S. S.; Kaufman, J. L.; Van der Ven, A. CASM — A software package for first-principles based study of multicomponent crystalline solids. *Nato. Sc. S. Ss. Iii. C. S.* **2023**, *217*, 111897.
(28) Van der Ven, A.; Thomas, J.; Puchala, B.; Natarajan, A. First-Principles Statistical Mechanics of Multicomponent Crystals. *Annu. Rev. Mater. Res.* **2018**, *48*, 27−55.
(29) Deng, Z.; Sai Gautam, G.; Kolli, S. K.; Chotard, J.-N.; Cheetham, A. K.; Masquelier, C.; Canepa, P. Phase Behavior in Rhombohedral NaSiCON Electrolytes and Electrodes. *Chem. Mater.* **2020**, *32*, 7908−7920.
(30) Pan, J.; Cordell, J. J.; Tucker, G. J.; Zakutayev, A.; Tamboli, A. C.; Lany, S. Perfect short-range ordered alloy with line-compound-like properties in the $ZnSnN_2$:ZnO system. *npj Comput. Mater.* **2020**, *6*, 1−6.
(31) Chevrier, V. L.; Ceder, G. Challenges for Na-ion Negative Electrodes. *J. Electrochem. Soc.* **2011**, *158*, A1011.
(32) Yu, S.-H.; Feng, X.; Zhang, N.; Seok, J.; Abruña, H. D. Understanding Conversion-Type Electrodes for Lithium Rechargeable Batteries. *Acc. Chem. Res.* **2018**, *51*, 273−281.
(33) Boukamp, B. A.; Lesh, G. C.; Huggins, R. A. All-Solid Lithium Electrodes with Mixed-Conductor Matrix. *J. Electrochem. Soc.* **1981**, *128*, 725.
(34) Qiao, S.; Zhou, Q.; Ma, M.; Liu, H. K.; Dou, S. X.; Chong, S. Advanced Anode Materials for Rechargeable Sodium-Ion Batteries. *ACS Nano* **2023**, *17*, 11220−11252.
(35) Chan, C. K.; Peng, H.; Liu, G.; McIlwrath, K.; Zhang, X. F.; Huggins, R. A.; Cui, Y. High-performance lithium battery anodes using silicon nanowires. *Nat. Nanotechnol.* **2008**, *3*, 31−35.
(36) Cui, Y. Silicon anodes. *Nat. Energy* **2021**, *6*, 995−996.
(37) Ni, J.; Zhu, X.; Yuan, Y.; Wang, Z.; Li, Y.; Ma, L.; Dai, A.; Li, M.; Wu, T.; Shahbazian-Yassar, R.; Lu, J.; Li, L. Rooting binder-free tin nanoarrays into copper substrate via tin-copper alloying for robust energy storage. *Nat. Commun.* **2020**, *11*, 1212.
(38) Ni, J.; Li, X.; Sun, M.; Yuan, Y.; Liu, T.; Li, L.; Lu, J. Durian-Inspired Design of Bismuth−Antimony Alloy Arrays for Robust Sodium Storage. *ACS Nano* **2020**, *14*, 9117−9124.
(39) Kresse, G.; Furthmüller, J. Efficiency of ab-initio total energy calculations for metals and semiconductors using a plane-wave basis set. *Comput. Mater. Sci.* **1996**, *6*, 15−50.
(40) Kresse, G.; Furthmüller, J. Efficient iterative schemes for ab initio total-energy calculations using a plane-wave basis set. *Phys. Rev. B* **1996**, *54*, 11169−11186.
(41) Perdew, J. P.; Burke, K.; Ernzerhof, M. Generalized Gradient Approximation Made Simple. *Phys. Rev. Lett.* **1996**, *77*, 3865−3868.
(42) Wang, Z.; Park, S.; Deng, Z.; Carlier, D.; Chotard, J.-N.; Croguennec, L.; Gautam, G. S.; Cheetham, A. K.; Masquelier, C.; Canepa, P. Phase stability and sodium-vacancy orderings in a NaSICON electrode. *J. Mater. Chem. A* **2021**, *10*, 209−217.
(43) Blöchl, P. E. Projector augmented-wave method. *Phys. Rev. B* **1994**, *50*, 17953−17979.
(44) Kresse, G.; Joubert, D. From ultrasoft pseudopotentials to the projector augmented-wave method. *Phys. Rev. B* **1999**, *59*, 1758−1775.
(45) Monkhorst, H. J.; Pack, J. D. Special points for Brillouin-zone integrations. *Phys. Rev. B* **1976**, *13*, 5188−5192.

https://doi.org/10.1021/acs.chemmater.4c00592
Chem. Mater. XXXX, XXX, XXX−XXX